ACS APPLIED MATERIALS & INTERFACES

Research Article

www.acsami.org

Ultrathin Nanosheets of Organic-Modified β-Ni(OH)$_2$ with Excellent Thermal Stability: Fabrication and Its Reinforcement Application in Polymers

Saihua Jiang,*[,†] Zhou Gui,[‡] Guohua Chen,*[,†] Dong Liang,[§] and Jahangir Alam[†]

[†]School of Mechanical and Automotive Engineering, South China University of Technology, Wushan Road 381, Guangzhou 510641, P. R. China

[‡]State Key Laboratory of Fire Science, University of Science and Technology of China, Jinzhai Road 96, Hefei, Anhui 230027, P. R. China

[§]Key Lab of Fire Science and Technology of Guangdong Province, Sun Yat-sen University, Guangzhou, Guangdong 510006, P. R. China

Supporting Information

ABSTRACT: β-Nickel hydroxide (β-Ni(OH)$_2$), which combines two-dimensional (2D) structure and the catalytic property of nickel-containing compounds, has shown great potential for the application in polymer nanocomposites. However, conventional β-Ni(OH)$_2$ exhibits large thickness, poor thermal stability, and irreversible aggregation in polymer matrices, which limits its application. Here, we use a novel phosphorus-containing organosilane to modify the β-Ni(OH)$_2$ nanosheet, obtaining a new β-Ni(OH)$_2$ ultrathin nanosheet with excellent thermal stability. When compared to pristine β-Ni(OH)$_2$, the organic-modified β-Ni(OH)$_2$ (M-Ni(OH)$_2$) maintains nanosheet-like structure, and also presents a small thickness of around 4.6 nm and an increased maximum degradation temperature by 41 °C. Owing to surface organic-modification, the interfacial property of M-Ni(OH)$_2$ nanosheets is enhanced, which results in the exfoliation and good distribution of the nanosheets in a PMMA matrix. The addition of M-Ni(OH)$_2$ significantly improves the mechanical performance, thermal stability, and flame retardancy of PMMA/M-Ni(OH)$_2$ nanocomposites, including increased storage modulus by 38.6%, onset thermal degradation temperature by 42 °C, half thermal degradation temperature by 65 °C, and decreased peak heat release rate (PHRR) by 25.3%. Moreover, it is found that M-Ni(OH)$_2$ alone can catalyze the formation of carbon nanotubes (CNTs) during the PMMA/M-Ni(OH)$_2$ nanocomposite combustion, which is a very helpful factor for the flame retardancy enhancement and has not been reported before. This work not only provides a new 2D ultrathin nanomaterial with good thermal stability for polymer nanocomposites, but also will trigger more scientific interest in the development and application of new types of 2D ultrathin nanomaterials.

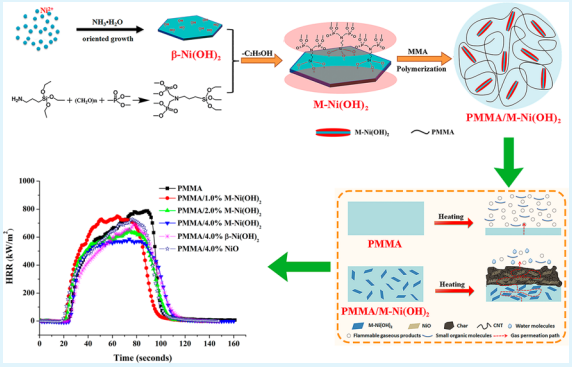

KEYWORDS: *β-Ni(OH)$_2$ ultrathin nanosheets, organically modification, interface property, catalytic effect, polymer nanocomposites, thermal stability, flame retardancy, mechanical performance*

1. INTRODUCTION

Recently, two-dimensional (2D) ultrathin nanosheets represented by graphene have received tremendous attention as their quantum size effects brought unique physical properties.[1−3] Beyond graphene itself, various 2D nanomaterials with graphene-like structure such as hexagonal boron nitride (h-BN), carbon nitrides (C_3N_4), metal chalcogenides (e.g., TiS_2, VS_2, and MoS_2), and metal oxides (e.g., MnO_2, SnO_2) have also been developed and show great potential for applications in supercapacitors, sensors, stamp-transferrable electrodes, transistors, catalysts, and polymer nanocomposites.[4−10] Especially for the polymer nanocomposite field, small amounts of the ultrathin 2D nanomaterials such as graphene, MoS_2, C_3N_4, etc. introduced into polymer matrices could significantly enhance the performances of polymer nanocomposites including optical, electronic, thermal, mechanical, or other physicochemical properties.[9−11] These performances are achieved, not only by using the inherent properties of the 2D nanomaterials, but also more importantly by their unique 2D structure, ultrathin thickness, and high specific surface areas.

Conventional β-Ni(OH)$_2$ has a well-ordered structure which consists of an ordered stacking of well-oriented β-Ni(OH)$_2$ nanosheets.[12] The β-Ni(OH)$_2$ nanosheet, similar to a graphene nanosheet, has strong stiffness, high specific surface areas, and

Received: January 27, 2015
Accepted: June 19, 2015
Published: June 19, 2015

DOI: 10.1021/acsami.5b04142
ACS Appl. Mater. Interfaces 2015, 7, 14603−14613

Scheme 1. Schematic Illustration for Preparation of PMMA/M-Ni(OH)$_2$ Nanocomposites: (a) Reaction Process and Structure for TMSAP and (b) in Situ Polymerization Process of PMMA/M-Ni(OH)$_2$ Nanocomposites

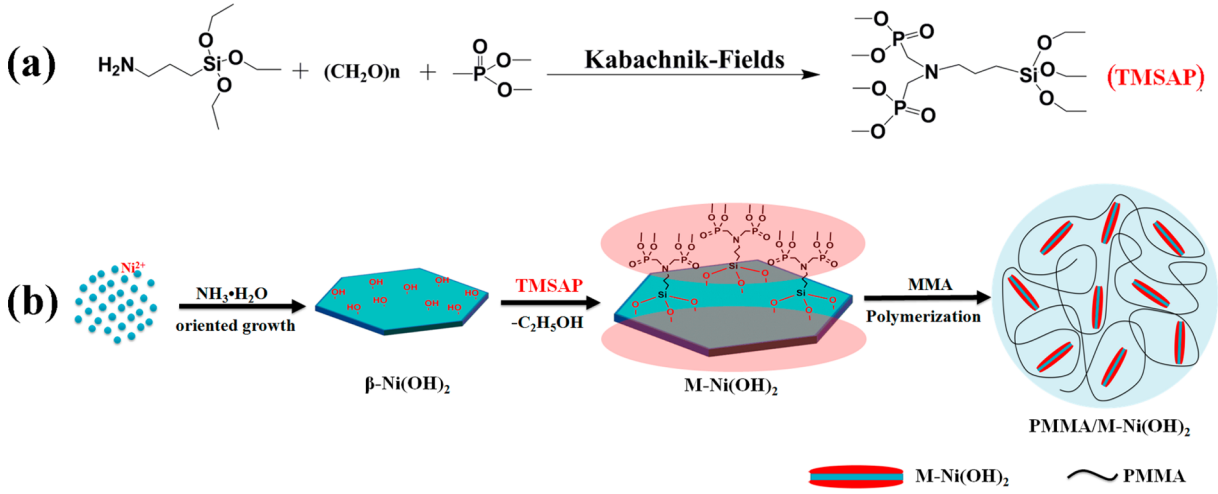

ultrathin thickness (~1 nm).[12−16] These properties make it a promising candidate for reinforcement application in polymer nanocomposites. In addition, nickel-containing compounds are a class of excellent catalysts. In addition to the application of photocatalytic water oxidation, CO catalytic oxidation, catalytic removal of toxic gas, etc., the catalytic charring effect of nickel-containing compounds in polymers was also reported.[17−20] During the combustion of polymers [polypropylene (PP), polystyrene (PS), polybuthylenesuccinate (PBS), etc.], the nickel-based compounds could catalyze the formation of carbon nanotubes (CNTs) from the polymers' degradation.[21−26] The as-obtained CNTs with high thermal stability and high strength could form jammed networks in the polymer matrix, which improves the thermal stability of polymers by increasing viscosity of melts, and reduces the flammability of polymers through inhibiting the evaporation of gaseous flammable components.[27] However, apart from nickel-containing compounds, the exotic layered nanomaterials are also required during the process of CNT formation. The addition of layered nanomaterials such as clay into polymers could increase the contact time of pyrolytic products and nickel catalyst through forming a maze or tortuous path, which is beneficial to the productivity of CNTs.[21−26] Owing to the combination of the advantages of 2D ultrathin nanomaterials and nickel-based compounds in β-Ni(OH)$_2$ nanosheet, these materials have the potential to catalyze the formation of CNTs without exotic layered compounds. On the basis of all of the analyses above, it is anticipated that the β-Ni(OH)$_2$ ultrathin nanosheet would benefit the mechanical, thermal, and flame-retardant property enhancements of polymer nanocomposites.

However, the β-Ni(OH)$_2$ nanosheets have some disadvantages which impede applications in polymers. First, the perfect stacking of the stoichiometric Ni(OH)$_2$ nanosheets in β-Ni(OH)$_2$ results in its very small interlayer spacing (4.60 Å) with a narrow space which does not allow the disengagement of its single layers through the anion exchange required exfoliation strategy.[13] Therefore, it is difficult to synthesize β-Ni(OH)$_2$ ultrathin nanosheets. Second, the onset decomposition temperature of pristine β-Ni(OH)$_2$ nanosheet (220 °C) is lower than processing temperatures of many polymers, unfavorable to the processing of polymer composites. Third, owing to the high surface energy resulting from their huge surface area, and hydrogen-bonding between nanosheets, the β-Ni(OH)$_2$ nanosheets tend to aggregate in polymer matrices.[12−16] The poor distribution of the nanosheets would have an adverse influence on polymer properties. Those are the reasons that only a few people until now have reported the application of β-Ni(OH)$_2$ nanosheets in polymers. For the synthesis of β-Ni(OH)$_2$ ultrathin nanosheets, some researchers have done a lot of work. For instance, Liang et al. prepared an ultrathin β-Ni(OH) nanosheet with thickness in the range 12−20 nm using nickel acetate as the nickel source and aqueous ammonia as a complexing reagent.[28] Li et al. have synthesized some β-Ni(OH) ultrathin nanosheets with thicknesses 1−15 nm via electrochemical reaction, and demonstrated that the NH_3 molecules could facilitate the formation of β-Ni(OH) ultrathin nanosheets.[15] On the basis of these references, in our previous work, β-Ni(OH)$_2$ ultrathin nanosheets with thicknesses of 2−4 nm have been successfully prepared via a facile method, with the aqueous ammonia and $NiCl_2$ dilute solution as the reagents.[29] Organic-modification provides a good solution for the enhancements of the dispersion, interface chemistry, and thermal stability of inorganic nanosheets. If organic molecules with high thermal stability were successfully grafted to the surface of the β-Ni(OH)$_2$ nanosheet by the organic-modification method, there will be a strong possibility to simultaneously enhance the distribution of β-Ni(OH)$_2$ nanosheets in the matrix and postpone the degradation of β-Ni(OH)$_2$ nanosheets. Because the organic molecules on the surface could not only enhance the compatibility between nanosheets and polymer matrix, but also protect the β-Ni(OH)$_2$ nanosheet from rapid decomposition by suppressing heat and mass transfer.

Inspired by the aforementioned concepts, in this work, an ultrathin β-Ni(OH)$_2$ nanosheet was first synthesized. The β-Ni(OH)$_2$ nanosheet contains free hydroxyl functional groups on the outside planes, which could dehydrate with silane coupling agents in the presence of catalyst. Tetramethyl (3-(triethoxysilyl)propyl-azanediyl) bis(methylene) diphosphonate (TMSAP), a phosphorus-containing silane coupling agent, whose degradation could produce a compact and heat-resistant char,[30] was then applied to the surface modification of the ultrathin β-Ni(OH)$_2$ nanosheet. Owing to the protection of TMSAP, a novel modified β-Ni(OH)$_2$ ultrathin nanosheet (M-

DOI: 10.1021/acsami.5b04142
ACS Appl. Mater. Interfaces 2015, 7, 14603−14613

$Ni(OH)_2$) with enhanced thermal stability was successfully obtained. The results of atomic force microscopy (AFM), transmission electron microscopy (TEM), X-ray diffraction (XRD), and Fourier transform infrared spectroscopy (FTIR) reveal the structure and composition of M-$Ni(OH)_2$. PMMA, a typical linear polymer, was chosen as the polymeric matrix. Due to the organic-modification, the interfacial property of M-$Ni(OH)_2$ was also enhanced, resulting in good dispersion of M-$Ni(OH)_2$ nanosheets in the PMMA matrix. Neat PMMA exhibits a moderate mechanical property, poor thermal stability, and high flammability, and forms little residue during combustion. The addition of M-$Ni(OH)_2$ remarkably not only catalyzes the CNT formation during the nanocomposite combustion, but also improves the properties of PMMA/M-$Ni(OH)_2$ nanocomposites including mechanical property, flame retardancy, and thermal stability. The detailed mechanisms of property enhancements are proposed.

2. EXPERIMENTAL SECTION

2.1. Raw Materials. Dimethyl phosphate (DMPP) was obtained from the Kaijie chemical company. Nickel chloride ($NiCl_2·6H_2O$), ammonium hydroxide ($NH_3·H_2O$), 3-aminopropylmethyldimethoxysilane (APTES), paraformaldehyde, tetrahydrofuran (THF), benzoyl peroxide (BPO), methyl methacrylate (MMA), and *N*,*N*′-dicyclohexylcarbodiimide (DCC, 99%) purchased from Sinopharm Chemical Reagent Co., Ltd. were of analytical grade. MMA, DMPP, and APTES were purified by reduced pressure distillation before use. BPO was further purified by recrystallization from methanol. THF was refluxed with natrium and then distilled before use. All other chemicals were used as received.

2.2. Synthesis of TMSAP. TMSAP is a new phosphorus-containing silane coupling agent.[30] Scheme 1a presents the synthesis procedure of TMSAP. Typically, paraformaldehyde (6.0 g, 0.20 mol), THF (40 mL), and APTES (22.1 g, 0.10 mol) were introduced into a 150 mL three-necked flask equipped with an addition funnel and a mechanical stirrer. The reaction mixture was stirred vigorously at 40 °C. DMPP (22.0 g, 0.20 mol) was then added dropwise within 3 h. The reaction was heated at 65 °C around for 12 h and then rotary evaporated to remove the solvent. The TMSAP was obtained with 80% yield as a viscous lemon yellow liquid.

FTIR (KBr, cm^{-1}): 2959−2854 (ν_{C-H}), 1460 (δ_{C-H}), 1250 ($\nu_{P=O}$), 1184 (ν_{C-N}), 1100 (ν_{Si-O}), 1015 (ν_{P-O}). ^{1}H NMR (400 MHz, $CDCl_3$-*d*, ppm): 0.53 (2H, −Si−CH_2−), 1.07 (9H, C−CH_3), 1.46 (2H, C−CH_2−C), 2.65 (2H, N−CH_2−), 3.09 (4H, N−CH_2−P), 3.45 (6H, O−CH_2−C), 3.6 (12H, O−CH_3). ^{31}P NMR (400 MHz, $CDCl_3$-*d*, ppm): 27.0 (s).

2.3. Preparation of *β*-$Ni(OH)_2$ Ultrathin Nanosheets. The *β*-$Ni(OH)_2$ ultrathin nanosheet was synthesized using a facile method. In a typical procedure, 50 mL of NH_3 aqueous solution (0.075 M) was added to 50 mL of $NiCl_2·6H_2O$ aqueous solution (0.05 M) under vigorous stirring at 60 °C. After 24 h of reaction, the final product was collected by centrifuging the above mixture, washed with water and ethanol many times, and then dried in a vacuum oven at 50 °C for 6 h for further characterization.

2.4. Preparation of M-$Ni(OH)_2$ Ultrathin Nanosheets. The M-$Ni(OH)_2$ ultrathin nanosheet was prepared by organic-modification of the *β*-$Ni(OH)_2$ nanosheet. Figure 1b shows the synthesis process of M-$Ni(OH)_2$ ultrathin nanosheets. Briefly, the *β*-$Ni(OH)_2$ nanosheets were first dispersed in TMSAP (400 mL) by vigorous stirring and ultrasonication for 2 h. The suspension of *β*-$Ni(OH)_2$ nanosheets was left to equilibrate for 1 h to allow any insoluble material or aggregates to precipitate. The precipitation was then removed, and the translucent milky green supernatant fraction was retained. Next, DCC (100 mg, as cat.) was added into the above suspension, and the mixture was then stirred and heated to 75 °C for 12 h. Finally, the resulting TMSAP-modified *β*-$Ni(OH)_2$ nanosheets (M-$Ni(OH)_2$) were centrifuged, washed with deioned water and ethanol, and then dried under vacuum overnight.

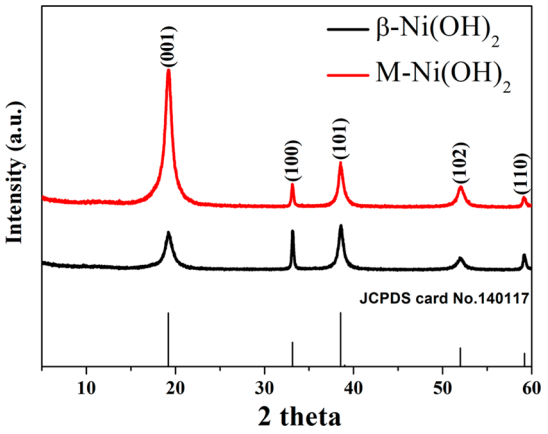

Figure 1. XRD patterns of *β*-$Ni(OH)_2$ and M-$Ni(OH)_2$ ultrathin nanosheets.

2.5. Preparation of PMMA/M-$Ni(OH)_2$ Nanocomposites. PMMA/M-$Ni(OH)_2$ nanocomposites were prepared using in situ bulk polymerization method, as illustrated in Figure 1b. Appropriate M-$Ni(OH)_2$ was first dispersed in 30 g of MMA monomers through vigorous stirring for 6 h. A 0.1 g portion of BPO was then added into the mixture at 85 °C. The mixture was kept at 85 °C and further stirred until it formed a viscous paste. Afterward, the paste was transferred into a mold and held at 50 °C for 48 h to complete the polymerization process. The loadings of M-$Ni(OH)_2$ nanosheets in all samples are summarized in Table 1.

Table 1. Compositions and Molecular Weights of PMMA and Its Composites

sample	component	M_n (g/mol) × 10^4	M_w (g/mol) × 10^4	polydispersity index
PMMA	neat PMMA	16.8	36.0	2.1
PMMA/1.0% M-$Ni(OH)_2$	1.0 wt % M-$Ni(OH)_2$	16.5	36.3	2.2
PMMA/2.0% M-$Ni(OH)_2$	2.0 wt % M-$Ni(OH)_2$	16.1	35.4	2.2
PMMA/4.0% M-$Ni(OH)_2$	4.0 wt % M-$Ni(OH)_2$	15.4	35.4	2.3
PMMA/4.0% *β*-$Ni(OH)_2$	4.0 wt % *β*-$Ni(OH)_2$	15.9	36.6	2.3
PMMA/4.0% NiO	4.0 wt % amorphous NiO	16.2	35.6	2.2

For comparison, pristine *β*-$Ni(OH)_2$ nanosheets and amorphous NiO particles were incorporated into PMMA matrix by the method used above. The composition of the samples is also given in Table 1.

2.6. Characterization. ^{1}H NMR and ^{31}P NMR analyses of the synthetic monomer were carried out on an AVANCE 400 Bruker spectrometer, and chloroform-*d* was used as the solvent.

XRD was performed by a Japan Rigaku D/Max-*γ*A rotation anode X-ray diffractometer equipped with graphite monochromatized Cu K*α* radiation (λ = 1.541 78 Å).

Molecular weights were determined by gel permeation chromatography (GPC) with a Waters 410 differential refractometer. THF (high-pressure liquid chromatographic grade) was used as the eluant at a flow rate of 1 mL/min.

Dynamic mechanical analysis (DMA) of nanocomposites was conducted on a DMA Q800 (TA Instruments Inc.) from room temperature to 170 °C at a linear heating of 5 °C/min (fixed frequency: 10 Hz).

The tensile strength at breaking was measured according to the Chinese standard method (GB 13022-91) with a WD-20D electronic

DOI: 10.1021/acsami.5b04142
ACS Appl. Mater. Interfaces 2015, 7, 14603−14613

universal testing instrument at a crosshead speed of 50 mm/min. Each sample was measured five times.

AFM was employed to observe β-Ni(OH)$_2$ and M-Ni(OH)$_2$ using a Veeco DI Multimode V scanning probe microscope.

TEM and high-resolution transmission electron microscopy (HRTEM) images were conducted on a JEOL JEM-2100F transmission electron microscopy with 200 keV accelerated voltage, in conjunction with a system of energy dispersive X-ray spectroscopy (EDX) analysis.

Scanning electron microscopy (SEM) images were carried out on a FEI Co. Ltd. Sirion200 scanning electron microscope at 5 kV acceleration voltages.

Thermogravimetric analysis (TGA) was recorded by a Q5000 thermoanalyzer instrument (TA Instruments Inc.) at a linear heating rate of 10 °C/min. The amount of grafted TMSAP was calculated by eq 1:[31]

$$\text{grafted amount(mequiv/g)} = \frac{10^3 W_{50-600}}{(100 - W_{50-600})M} \quad (1)$$

Here, M (g/mol) is the molecular weight of TMSAP (M = 465), and W_{50-600} is the weight loss between 50 and 600 °C corresponding to degradation of TMSAP.

Cone calorimeter test (CCT) was carried out on a Stanton Redcroft cone calorimeter according to ISO 5560 standard, with a heat flux of 35 kW/m^2.

Limiting oxygen index (LOI) values were measured by LOI Analyzer instrument, according to the ASTM standard D2863.

FTIR spectra were carried out on a Nicolet 6700 spectrometer, as described in ref 30.

Raman spectroscopy (RS) measurements were recorded on a SPEX-1403 laser Raman spectrometer with excitation using a 514.5 nm argon laser line in the backscattering geometry.

3. RESULTS AND DISCUSSION

3.1. Characterization of β-Ni(OH)$_2$ and M-Ni(OH)$_2$ Nanosheets. The crystal structure and phase purity of β-Ni(OH)$_2$ and M-Ni(OH)$_2$ nanosheets were characterized by XRD. Figure 1a displays the typical XRD pattern of pure β-Ni(OH)$_2$ nanosheet, in which all the peaks can be readily indexed to hexagonal β-Ni(OH)$_2$ (space group $P\bar{3}m1$, $a = b =$ 3.126 Å, c = 4.605 Å, $\alpha = \beta = 90°$, $\gamma = 120°$; JCPDS card no. 14-0117), suggesting the high purity of the obtained sample. The intense and sharp diffraction peaks demonstrate that the product is well-crystallized. After modification by TMSAP, the characteristic peaks of β-Ni(OH)$_2$ such as (001), (100), (101), (102), and (110) peaks are kept in the patterns of M-Ni(OH)$_2$, reflecting that the 2D crystal structure of M-Ni(OH)$_2$ ultrathin nanosheets is mostly preserved and not affected significantly by the modification.

The structure of β-Ni(OH)$_2$ and M-Ni(OH)$_2$ was also studied by TEM and AFM. TEM image of β-Ni(OH)$_2$ (Figure 2a) shows a large area of nearly transparent nanosheets with the lateral size 200−500 nm, which indicates the ultrathin nanosheet morphology of the as-fabricated β-Ni(OH)$_2$ nanosheets. The HRTEM image of β-Ni(OH)$_2$ (Figure 2b) reveals the nature of the hexagonal crystal nanosheet with a [101] preferential orientation. In addition, the edge-area HRTEM image (Figure 2c) gives solid evidence that the β-Ni(OH)$_2$ nanosheets are ultrathin nanostructures with a height of 2.70 nm. The thickness of the β-Ni(OH)$_2$ nanosheet was also evaluated by AFM. From the AFM image and the corresponding height profiles (Figure 3a,b), the measured height of β-Ni(OH)$_2$ nanosheets is around 3.0 nm, consistent with the edge-area HRTEM measurement. These results illustrate the successful synthesis of high-quality β-Ni(OH)$_2$ ultrathin nanosheets. Figure 2d is the TEM image of M-Ni(OH)$_2$, displaying the nanosheet morphology of M-Ni(OH)$_2$. As illustrated in Figure 2e, the HRTEM image of M-Ni(OH)$_2$ nanosheets also shows a [101] orientation, which implies that the hexagonal crystal structure of β-Ni(OH)$_2$ is maintained during the modification process. That is in agreement with the XRD analysis. However, compared with the smooth surface of pristine β-Ni(OH)$_2$ nanosheets, the surface of M-Ni(OH)$_2$ becomes coarser, which may be attributed to the graft of TMSAP on the surface. To prove this point, EDX analysis of M-Ni(OH)$_2$ was also carried out (Figure 2f), from which the elements of nitrogen, silicon, and phosphorus can be identified on the surface of M-Ni(OH)$_2$. Moreover, the AFM image of M-Ni(OH)$_2$ (Figure 3c,d) depicts an increased thickness of the M-Ni(OH)$_2$ nanosheet (4.6 nm) when compared to the β-Ni(OH)$_2$ ultrathin nanosheet. This thickness increase further confirms the presence of TMSAP on the M-Ni(OH)$_2$ nanosheet surface.[32] The above characterization results clearly demonstrate the successful synthesis of M-Ni(OH)$_2$ ultrathin nanosheets through organic-modification of β-Ni(OH)$_2$ nanosheets.

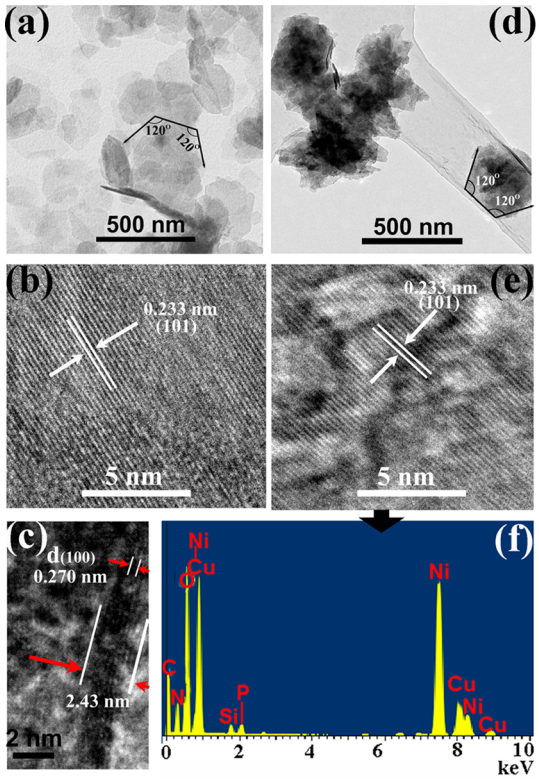

Figure 2. (a) TEM image and (b) HRTEM image of β-Ni(OH)$_2$ ultrathin nanosheets; (c) HRTEM image of the edge of a β-Ni(OH)$_2$ ultrathin nanosheet; (d) TEM image, (e) HRTEM image, and (f) EDX spectra of M-Ni(OH)$_2$ ultrathin nanosheets.

Figure 4 presents the FTIR spectra of TMSAP, β-Ni(OH)$_2$, and M-Ni(OH)$_2$. For TMSAP, the bands at 2959−2854 and 1460 cm^{-1} correspond to the stretching vibration and deformation vibration of C—H, respectively; the band at 1184 cm^{-1} is assigned to C—N, and the bands at 1250 and 1015 cm^{-1} are assigned to P═O and P—O, respectively. The band at 1100 cm^{-1} corresponds to Si—O—R stretching vibration.[30] For pristine β-Ni(OH)$_2$, the FTIR spectrum also exhibits several characteristic absorption bands including 3430 and 1631 cm^{-1} (vibrations of hydrogen-bonded O—H located

DOI: 10.1021/acsami.5b04142
ACS Appl. Mater. Interfaces 2015, 7, 14603−14613

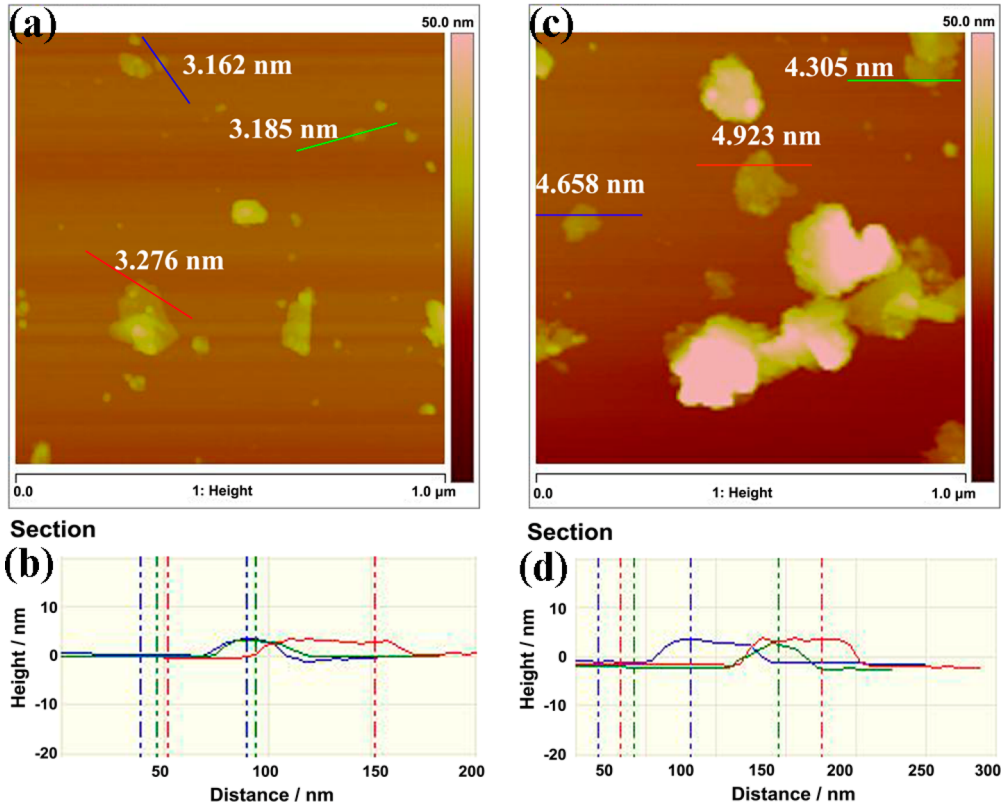

Figure 3. (a) AFM image and (b) the corresponding height profile of β-Ni(OH)$_2$ ultrathin nanosheets; (c) AFM image and (d) the corresponding height profile of M-Ni(OH)$_2$ ultrathin nanosheets.

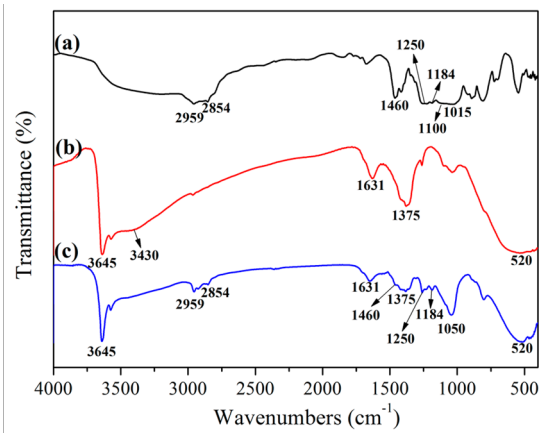

Figure 4. FTIR spectra: (a) TMSAP, (b) β-Ni(OH)$_2$, and (c) M-Ni(OH)$_2$.

on the surface of β-Ni(OH)$_2$ nanosheet), 3645 cm^{-1} (stretching vibration of non-hydrogen-bonded free O—H of the brucite-like sheet structure), and 520 cm^{-1} (in plane deformation mode of free O—H). The peak at 1375 cm^{-1}, corresponding to the vibration of CO_3^{2-}, is ascribed to the absorption of CO_2 in β-Ni(OH)$_2$.[33] By organic-modification, most characteristic bands of β-Ni(OH)$_2$ are kept in M-Ni(OH)$_2$, implying the structural integrity of nanosheet, consistent with XRD and TEM results. Nevertheless, new FTIR peaks assigned to TMSAP, such as C—H vibrations at 2959−2854 and 1460 cm^{-1}, P═O vibration at 1250 cm^{-1}, and C—N vibration at 1184 cm^{-1}, can also be observed in the spectrum, suggesting the existence of TMSAP in M-Ni(OH)$_2$. Additionally, the relative intensities of peaks at 3430, 1631, and 1375 cm^{-1} are decreased, indicating the reduction of the absorbed CO_2, and hydrogen-bonded O—H on the surface, which is due to the participation of O—H in the organic-modification and the decreased polarity of β-Ni(OH)$_2$ nanosheets that results.[31,34] The interfacial property change, which can improve the compatibility between the nanosheets and polymer matrices, is conducive to the dispersion of the nanosheets. The peak at 1050 cm^{-1} is attributed to the Si—O—Ni group, which is formed by the reaction between silane and −OH. These results provide direct evidence for the reaction of TMSAP and β-Ni(OH)$_2$ nanosheets, further demonstrating the successful modification of β-Ni(OH)$_2$.

TGA and differential thermogravimetric (DTG) curves of TMSAP, β-Ni(OH)$_2$, and M-Ni(OH)$_2$ in nitrogen flows are presented in Figure 5. The thermal decomposition of TMSAP occurs in two stages. The first stage before 330 °C is attributed to the degradation of phosphite ester groups, while the second stage from 330 to 600 °C is ascribed to the decomposition of alkoxy groups.[35] From Figure 5, the degradation of TMSAP has a high char yield, equal to 52.6 wt %. In the case of pristine β-Ni(OH)$_2$ nanosheets, the main mass loss stage from 200 to 400 °C is ascribed to the dehydration, leaving 78.5 wt % NiO nanolayers in the end.[36] After modification by TMSAP, the dehydration of M-Ni(OH)$_2$ is postponed. In detail, the maximum loss temperature of M-Ni(OH)$_2$ is 324 °C, which is 41 °C higher than that of β-Ni(OH)$_2$ (283 °C). That is because the thermally stable char formed by the degradation of TMSAP prevents the β-Ni(OH)$_2$ nanosheets from further degradation. Moreover, from Figure 5, the degradation of M-Ni(OH)$_2$ between 330 and 600 °C is consistent with that of TMSAP, which further confirms that the TMSAPs have been grafted onto the surface of the M-Ni(OH)$_2$ nanosheets. The

DOI: 10.1021/acsami.5b04142
ACS Appl. Mater. Interfaces 2015, 7, 14603−14613

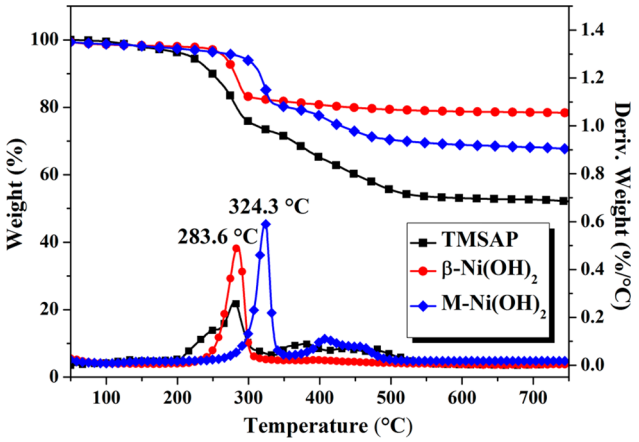

Figure 5. TGA and DTG curves of TMSAP, β-Ni(OH)$_2$, and M-Ni(OH)$_2$ in N_2.

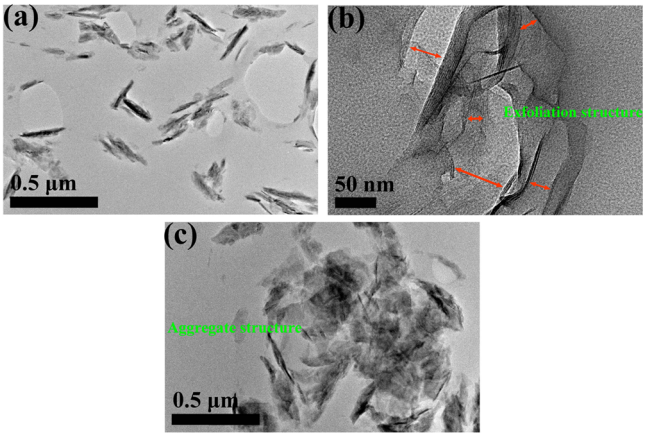

Figure 6. TEM images: (a, b) PMMA/4.0% M-Ni(OH)$_2$ at different magnifications; (c) PMMA/4.0% β-Ni(OH)$_2$ at low magnification.

grafted amount of M-Ni(OH)$_2$ sample is 2.39 mmol/g by calculation.[31] According to the characterization above, we can conclude that a new organic-modified β-Ni(OH)$_2$ ultrathin nanosheet with higher thermal stability has been successfully prepared.

3.2. Characterization of PMMA/M-Ni(OH)$_2$ Nanocomposites. Molecule weight is an important structure parameter for polymers or polymer composites. To evaluate the molecule weights of PMMA/M-Ni(OH)$_2$ nanocomposites, all the nanocomposites were extracted with THF using a Soxhlet extractor. Each extracted polymer was characterized by GPC, and the corresponding M_w, M_n, and polydispersity index are listed in Table 1. From Table 1, the polymerization of MMA in the presence of M-Ni(OH)$_2$ results in the formation of PMMA/M-Ni(OH)$_2$ nanocomposites with slightly decreased molecular weight and increased polydispersity, in comparison with pure PMMA prepared under same condition in the absence of M-Ni(OH)$_2$. These results can be ascribed to the interference of the active sites on the M-Ni(OH)$_2$ surface that act as free radical scavengers and free radical traps; that is, the free radicals that form on the polymer chain transfer to the Lewis acid sites of the M-Ni(OH)$_2$ surface and hinder polymerization of MMA.[37,38] Thus, the addition of M-Ni(OH)$_2$ has a small negative influence on the molecule weights of the nanocomposites.

Internal morphology is another important structure parameter for polymer composites. To study the morphologic structure of PMMA/M-Ni(OH)$_2$ nanocomposites, TEM was employed. Figure 6 presents the representative TEM images of PMMA/M-Ni(OH)$_2$ nanocomposites (PMMA/4.0% M-Ni(OH)$_2$). From Figure 6a, at lower magnification, the M-Ni(OH)$_2$ nanosheets have lost their restacking structure and are uniformly dispersed in the matrix. At higher magnification (Figure 6b), the M-Ni(OH)$_2$ nanosheets are mostly exfoliated. For comparison, a TEM image of PMMA/4.0% β-Ni(OH)$_2$ composite was also displayed in Figure 6. From Figure 6c, the pristine β-Ni(OH)$_2$ sheets without modification aggregate severely in the matrix, and few exfoliated β-Ni(OH)$_2$ sheets can be observed. Thus, the success of molecular level dispersion of M-Ni(OH)$_2$ nanosheets in the nanocomposite is due to the organic-modification, as a result of which the TMSAP molecules linked to nanosheets are more compatible with the matrix than pristine nanosheets. During in situ copolymerization, the TMSAP molecules act as good compatibilizers to prevent the M-Ni(OH)$_2$ ultrathin nanosheets from reaggregating. On the basis of the TEM result, it is concluded that exfoliated PMMA/M-Ni(OH)$_2$ nanocomposites with good dispersion have been successfully prepared. The good dispersion and exfoliated structure are conducive to the property improvements listed below.

3.3. Mechanical Property of PMMA/M-Ni(OH)$_2$ Nanocomposites. To evaluate the mechanical properties of PMMA/M-Ni(OH)$_2$ nanocomposites, both DMA and tensile tests were employed, and the corresponding data are given in Table 2. The storage modulus versus temperature is plotted in Figure 7. As shown in Table 2 and Figure 7, the storage moduli of PMMA/M-Ni(OH)$_2$ are significantly enhanced by adding even a small amount of M-Ni(OH)$_2$ ($\leq$4.0 wt %). In detail, 1.0 wt % M-Ni(OH)$_2$ added into PMMA matrix (PMMA/1.0% M-Ni(OH)$_2$) increases storage modulus by 347 MPa. When more M-Ni(OH)$_2$ is introduced, the increment of storage modulus becomes bigger, leading to a 38.6% maximum increase in storage modulus of the nanocomposites (3089 MPa for PMMA/4.0% M-Ni(OH)$_2$). Tensile strength of PMMA/M-Ni(OH)$_2$ nanocomposites (Table 2) exhibits the same tendency as their storage modulus. With the addition of M-Ni(OH)$_2$, tensile strength of all nanocomposites becomes higher than that of pure PMMA, and increases as M-Ni(OH)$_2$ content rises. The largest increase of tensile strength is 31.0% (30.5 MPa for PMMA/4.0% M-Ni(OH)$_2$). These results above demonstrate the good reinforcement function of M-Ni(OH)$_2$ nanosheets for PMMA/M-Ni(OH)$_2$ nanocomposites. It appears that three factors influence the mechanical perform-

Table 2. Mechanical Performances of PMMA and Its Composites

sample	tensile strength (MPa)	elongation (%)	storage modulus (MPa)
PMMA	22.9 ± 1.2	3.5 ± 0.9	2228
PMMA/1.0% M-Ni(OH)$_2$	25.6 ± 1.9	4.5 ± 1.5	2575
PMMA/2.0% M-Ni(OH)$_2$	29.1 ± 1.7	4.0 ± 1.3	2868
PMMA/4.0% M-Ni(OH)$_2$	30.5 ± 2.0	3.5 ± 1.1	3089
PMMA/4.0% β-Ni(OH)$_2$	25.3 ± 0.9	2.0 ± 1.3	2433
PMMA/4.0% NiO	20.9 ± 1.6	2.0 ± 0.7	2301

DOI: 10.1021/acsami.5b04142
ACS Appl. Mater. Interfaces 2015, 7, 14603−14613

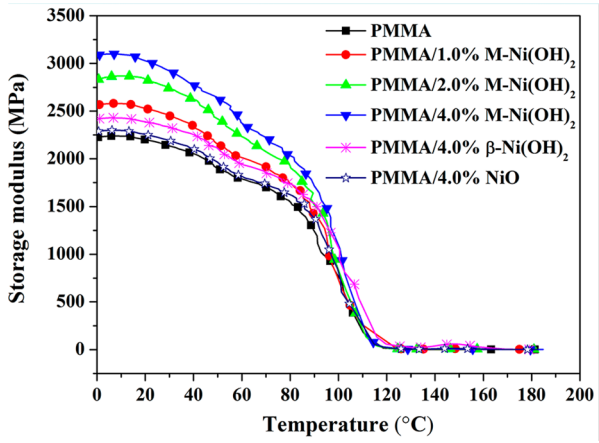

Figure 7. Plots of storage moduli versus temperatures for PMMA and its composites.

ances of nanocomposites: (a) the high stiffness of M-$Ni(OH)_2$ nanosheets, which is the root for the mechanical performance enhancements; (b) the interfacial interaction between the M-$Ni(OH)_2$ nanosheets and the PMMA matrix; and (c) the distribution of M-$Ni(OH)_2$ nanosheets in the PMMA matrix. To prove this point, the mechanical performances of PMMA/4.0% β-$Ni(OH)_2$ and PMMA/4.0% NiO were also investigated. As can be observed in Table 2, the introduction of 4.0 wt % β-$Ni(OH)_2$ and 4.0 wt % M-$Ni(OH)_2$ endows the composites with better mechanical performances than NiO particles, indicating the importance of 2D structure in the mechanical performance enhancement. The 2D ultrathin nanosheets possess larger specific surface areas than amorphous particles, which contributes to the enhancement of interfacial interaction between nanofiller and the matrix. In addition, at the same filler content, both tensile strength and storage modulus of PMMA/4.0% β-$Ni(OH)_2$ are much lower than those of PMMA/4.0% M-$Ni(OH)_2$. That may be ascribed to the poor dispersion of nanofillers in PMMA/4.0% M-$Ni(OH)_2$. According to the TEM results, pristine β-$Ni(OH)_2$ nanosheets tend to aggregate in the nanocomposites due to the strong intermolecular forces. The aggregation can cause an intensification of stress when subject to force. Fractures are apt to occur in these places. In the case of PMMA/M-$Ni(OH)_2$ nanocomposites, organic-modification of the M-$Ni(OH)_2$ ultrathin nanosheets improves the compatibility between the nanosheets and PMMA matrix, which exfoliates the M-$Ni(OH)_2$ nanosheets and enhances their dispersion in the matrix, and then results in increased specific surface areas of M-$Ni(OH)_2$. The increased specific surface area enhances the interfacial interactions. Therefore, strong interfacial interaction and good distribution of nanosheets are two key reasons for the further enhancement of mechanical performance of PMMA/M-$Ni(OH)_2$ nanocomposites.

To verify the existence of the strong interfacial interaction between the PMMA matrix and M-$Ni(OH)_2$ nanosheets, PMMA and PMMA/4.0% M-$Ni(OH)_2$ were cryogenically broken after immersion in liquid nitrogen, and the fractured surface was characterized by SEM (Figure 8). From Figure 8a, pure PMMA exhibits a smooth fracture surface, suggesting brittle failure of a homogeneous material. In comparison, the fracture surface of PMMA/M-$Ni(OH)_2$ is much coarser, and most M-$Ni(OH)_2$ nanosheets are embedded in the PMMA matrix, suggesting that M-$Ni(OH)_2$ nanosheets have strong interfacial adhesion with polymer matrix. Furthermore, it is

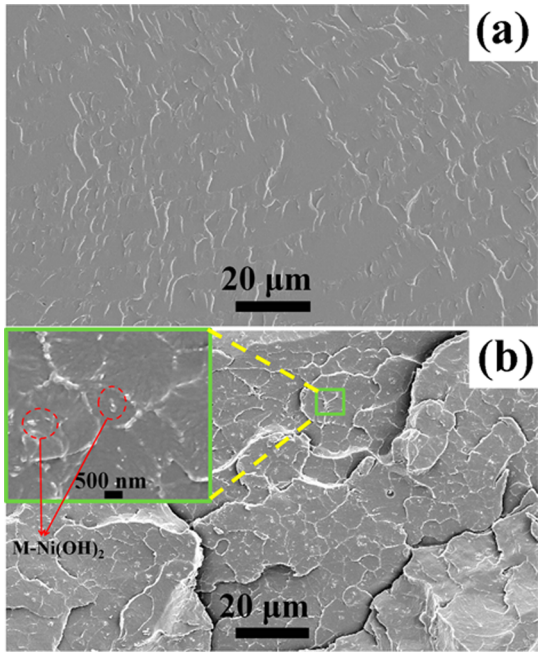

Figure 8. SEM images of the fractured surfaces: (a) PMMA and (b) PMMA/4.0% M-$Ni(OH)_2$.

evident that the M-$Ni(OH)_2$ nanosheets are distributed uniformly on the fracture surface of polymer, which is consistent with TEM results.

3.4. Thermal Stability of PMMA/M-$Ni(OH)_2$ Nanocomposites. Thermal stability of PMMA/M-$Ni(OH)_2$ nanocomposites was evaluated by TGA. Figure 9 illustrates the TGA

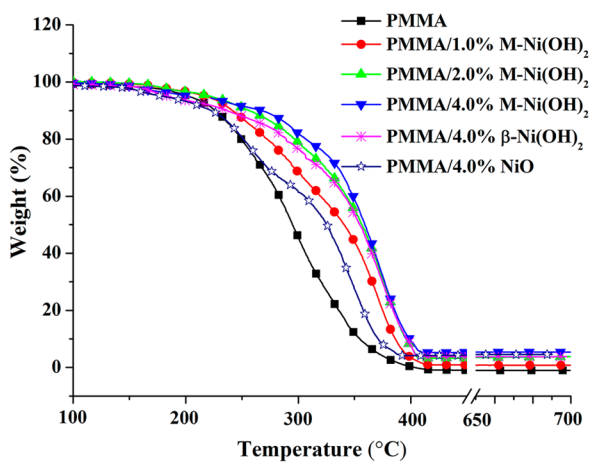

Figure 9. TGA curves of PMMA and the composites in air.

curve of PMMA and its composites in air flow, and the corresponding data are summarized in Table 3. As observed in Figure 9, the broad weight-loss step between 200 and 420 °C, corresponding to thermal degradation of the PMMA matrix, shifts to a higher temperature with the increasing M-$Ni(OH)_2$ loading. In detail, both initial degradation temperature ($T_{0.1}$) and half degradation temperature ($T_{0.5}$) of all PMMA/M-$Ni(OH)_2$ samples are higher than those of pure PMMA. For instance, the introduction of 4.0 wt % M-$Ni(OH)_2$ into PMMA matrix increases the $T_{0.1}$ by 42 °C and $T_{0.5}$ by 65 °C. These results suggest that the addition of M-$Ni(OH)_2$ remarkably

DOI: 10.1021/acsami.5b04142
ACS Appl. Mater. Interfaces 2015, 7, 14603−14613

Table 3. Thermal Properties and Flammability of PMMA and Its Composites

sample	$T_{0.1}$ (°C)	$T_{0.5}$ (°C)	residue (wt %)[a]	char (wt %)[b]	LOI (%)	PHRR (kW/m^2)	THR (MJ/m^2)
PMMA	226	295	0	0	17.0 ± 0.0	786 ± 21	44 ± 3
PMMA/1.0% M-Ni(OH)$_2$	242	341	0.9	0.1	18.0 ± 0.0	752 ± 7	42 ± 1
PMMA/2.0% M-Ni(OH)$_2$	257	357	3.4	1.8	18.5 ± 0.5	654 ± 26	40 ± 3
PMMA/4.0% M-Ni(OH)$_2$	268	359	5.4	2.2	20.0 ± 0.5	587 ± 20	39 ± 3
PMMA/4.0% β-Ni(OH)$_2$	236	341	4.5	1.2	19.0 ± 0.5	695 ± 32	40 ± 4
PMMA/4.0% NiO	226	325	4.6	0.6	18.0 ± 0.0	730 ± 13	41 ± 2

[a]Residue yield of the nanocomposites obtained from TGA at 700 °C. [b]Char yield of the nanocomposites obtained from TGA at 700 °C, minus the residue of M-Ni(OH)$_2$.

improves the thermal stability of PMMA. The physical barrier effect of M-Ni(OH)$_2$ nanosheets, which restricts the polymer chain movement and retards the transfer of gas products, is hypothesized to be an important reason for the improved thermal stability.[39,40] In addition, according to the earlier references, nickel-containing compounds could catalyze the char formation of polymers, such as PP, PBS, and PS.[21−26] The char formed on the surface during pyrolysis would retard the diffusion of mass and heat, and simultaneously reduce the production of gas products, which is another key factor for the thermal stability enhancement. This point can be confirmed by the greater char amount of composites after pyrolysis as compared to that of PMMA. From TGA curves and Table 3, pure PMMA has no residue at 700 °C, while the corresponding residue of PMMA/M-Ni(OH)$_2$ at 700 °C rises from 0.9 to 5.4 wt %, as the nanofiller content increases from 1.0 to 4.0 wt %. The residue amount is larger than what might be expected only on the basis of the M-Ni(OH)$_2$ content, suggesting that the residue of nanocomposites consists of both char from the polymer matrix as well as the M-Ni(OH)$_2$ residue. After the deduction of the residue from M-Ni(OH)$_2$, the char yields at 700 °C are also given in Table 3. The char amount of PMMA/M-Ni(OH)$_2$ nanocomposites rises with increasing M-Ni(OH)$_2$ content, confirming the catalytic charring effect of M-Ni(OH)$_2$ to PMMA matrix. Furthermore, compared to PMMA/4.0% NiO composite, both PMMA/4.0% β-Ni(OH)$_2$ and PMMA/4.0% M-Ni(OH)$_2$ exhibit a higher char amount, indicating that 2D nanosheet-like structure is positive to the catalytic charring effect of M-Ni(OH)$_2$. During the thermal degradation process of nanocomposites, 2D nanosheets are barriers for the transfer of pyrolytic product, acting as a sealed autoclave-like microreactor, which increases the contact time of pyrolytic products and nickel catalyst, and then promotes the catalytic property enhancement.[21,25] M-Ni(OH)$_2$ nanosheets combine a physical barrier effect and a catalytic charring effect; the thermal stability of PMMA/M-Ni(OH)$_2$ is thus significantly enhanced.

3.5. Flame Retardancy of PMMA/M-Ni(OH)$_2$ Nanocomposites. The catalytic charring effect and the physical barrier effect are also conducive to flame retardancy enhancement of polymers. LOI was used to evaluate the flame retardancy of PMMA/M-Ni(OH)$_2$ nanocomposites. Pure PMMA resin is highly flammable, and its LOI value is only 17.0%. With addition of M-Ni(OH)$_2$ ultrathin nanosheets, the LOI values of the nanocomposites increase gradually. As the M-Ni(OH)$_2$ content reaches 4.0 wt %, the corresponding LOI value of PMMA/M-Ni(OH)$_2$ nanocomposites increases to 20.0%, suggesting the good flame-retardant effect of M-Ni(OH)$_2$ nanosheets. To further investigate the flame retardancy of PMMA/M-Ni(OH)$_2$ nanocomposites, all samples were characterized by CCT. Heat release rate (HRR), PHRR, and total heat release (THR) obtained from CCT tests are three key parameters for fire hazard evaluation of materials; PHRR especially is regarded as the most important parameter.[41] Figure 10a shows the HRR curves of PMMA

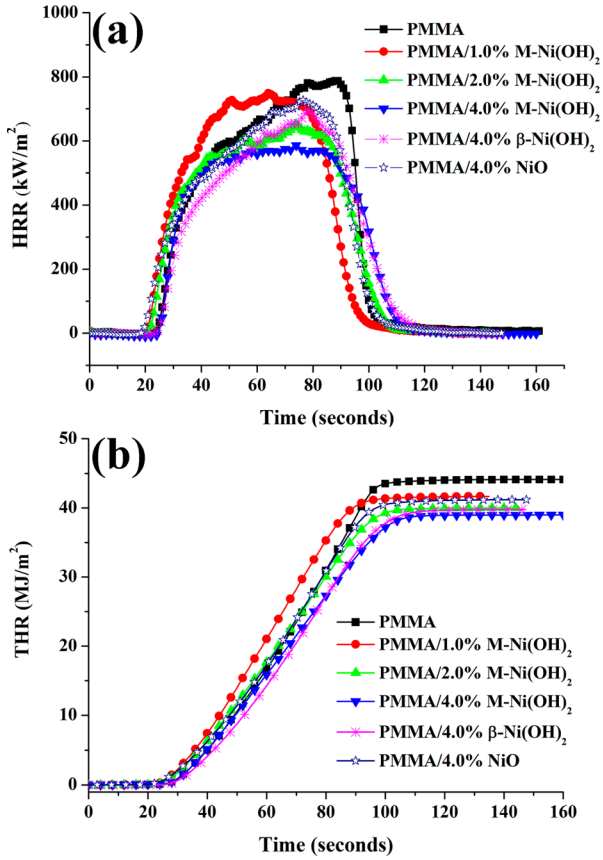

Figure 10. Combustibility of PMMA and the composites obtained from CCT test: (a) HRR curves vs time and (b) THR curves vs time.

and the composites versus temperatures. The corresponding THR values are plotted in Figure 10b. From Figure 10, the PHRR (786 kW/m^2) and THR (44 MJ/m^2) of PMMA are very high. With introduction of M-Ni(OH)$_2$ (≤4.0 wt %), both PHRR and THR of all PMMA/M-Ni(OH)$_2$ nanocomposites are shifted to lower values, and decrease as M-Ni(OH)$_2$ loading rises. The maximum decreases of PHRR and THR achieved in PMMA/4.0 wt % M-Ni(OH)$_2$ (587 kW/m^2 for PHRR, 39 MJ/m^2 for THR) are 25.3% and 11.4%, respectively. These results further confirm the good flame-retardant effect of M-Ni(OH)$_2$ on PMMA resin. On the basis of the LOI and CCT results, and the TGA analysis above, flame retardancy of the nanocomposites is mainly influenced by two factors: catalytic charring effect and physical barrier effect of M-Ni(OH)$_2$

DOI: 10.1021/acsami.5b04142
ACS Appl. Mater. Interfaces 2015, 7, 14603−14613

nanosheets. Owing to the catalysis of M-Ni(OH)$_2$ to the matrix, char is formed on the surface of samples during combustion, which acts as a stable protective layer to retard the transfer of heat, flammable gas products, and oxygen.[42] The flammability of the nanocomposites is thus reduced. For example, within the same filler content, the PMMA/4.0% M-Ni(OH)$_2$ produces more char during combustion than PMMA/4.0% β-Ni(OH)$_2$ and PMMA/4.0% NiO, and thus exhibits the best flame retardancy. On the other hand, the M-Ni(OH)$_2$ nanosheets degrade to NiO nanolayers at high temperature which can form a maze or "tortuous path" to barrier of the diffusion of flammable pyrolytic products. Both of these effects that occur in the condensed phase are beneficial to the flame retardancy.[25,43] In addition to the condensed phase mechanisms, the water molecules generated from M-Ni(OH)$_2$, which dilute the flammable gas products and cool down the fire temperature in the gas phase, are another favorable factor for the flame retardancy. The combination of these factors above determines the flame retardancy enhancement of the nanocomposites.[42]

3.6. Char Analysis. To further illustrate the flame-retardant mechanism of the PMMA/M-Ni(OH)$_2$ nanocomposites, the char residue of samples after the CCT test was also investigated. Figure 11 is the Raman spectra of the nanocomposite char residue, exhibiting two peaks at 1356 and 1591 cm^{-1}. The former peak (D band) represents disordered graphite or glassy carbons; the latter peak (G band) corresponds to the stretching vibration mode with E_{2g} symmetry in the aromatic layers of the graphite crystalline.[44] This result implies that the graphitized char is formed during the nanocomposite degradation. To obtain more detail concerning the graphitized char, it is further purified with hydrofluoric acid (HF) and nitric acid (HNO_3). After purification, the NiO nanolayers do not exist anymore. The structure of CNTs in the purified char is clearly observed by means of TEM (Figure 11b) and SEM (Figure 11c,d), which indicates that the introduction of M-Ni(OH)$_2$ promotes the formation of CNTs during the nanocomposite combustion. Generally, the CNT formation from polymer combustion needs two factors: nickel-containing compounds and 2D nanomaterials, in which the nickel-containing compound plays a catalyst role, while the 2D nanomaterial act as a sealed autoclave-like microreactor.[21,25] Here, the M-Ni(OH)$_2$ combines the advantages of 2D nanosheet-like structure and nickel-containing compounds, and thus promotes the CNT formation. According to the earlier references, CNTs in polymers can reduce the flammability of polymers by forming a network-structured protective layer.[27] Moreover, due to the existence of CNTs, the thermal stability and mechanical performance of the char are enhanced, which is helpful to improve the barrier effect of char layers during combustion.

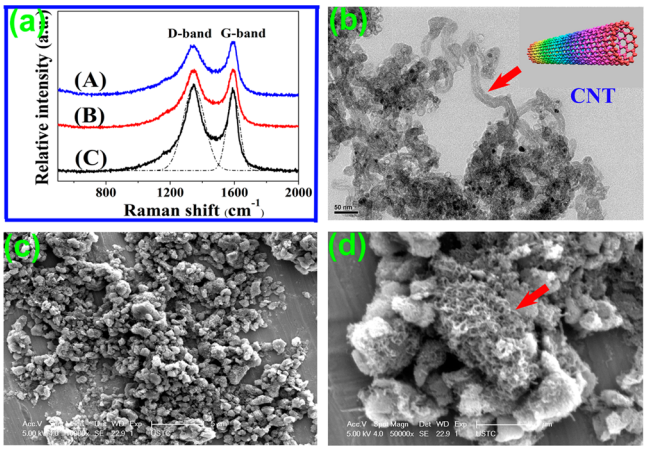

Figure 11. (a) Raman spectra for char residue of the nanocomposites: (A) PMMA/1.0% M-Ni(OH)$_2$, (B) PMMA/2.0% M-Ni(OH)$_2$, (C) PMMA/4.0% M-Ni(OH)$_2$; (b) TEM image and (c, d) SEM micrographs of PMMA/4.0% M-Ni(OH)$_2$ char residue purified by HF and HNO_3.

On the basis of the analysis above, we propose a suggested flame-retardant mechanism. A schematic representation of the mechanism is shown in Scheme 2. During the PMMA/M-Ni(OH)$_2$ nanocomposite combustion, some gaseous pyrolytic products such as CH_4 and C_3H_6 are released. Meanwhile, a protective charred ceramic surface layer is formed as the result of the ablative reassembly of the NiO sheets on the polymer surface, and the M-Ni(OH)$_2$ catalyzes the charring of the PMMA matrix. The char layers can inhibit the diffusion of flammable gas products into the flame zone and that of the O_2 and heat into the inner of polymers. Owning to the physical barrier effect of M-Ni(OH)$_2$ nanosheets, the nanosheets within nanocomposites can form a maze or "tortuous path" to slow down the volatilization of the gaseous pyrolytic products. In this case, the pyrolytic products have more time to contact the catalyst particles and are dehydrogenated and aromatized to form char containing a lot of CNTs since nickel is a good catalyst for CNT formation.[25] The as-obtained CNTs in the char further improve the flame-retardant effect of the char. On the other hand, the degradation of M-Ni(OH)$_2$ can produce water molecules. The water can dilute the flammable gas products and cool down the fire temperature in gas phase, which also is conducive to the enhancement of the flame retardancy.[44] The combination of the flame-retardant strategies above leads to the flame retardancy enhancement of PMMA/M-Ni(OH)$_2$ nanocomposites. When compared with other ultrathin nanosheets such as graphene and MoS_2 nanosheets, M-Ni(OH)$_2$ nanosheets in our work have been in the top class, if not the best, to enhance the mechanical performance, thermal stability, and flame retardancy of polymers. For instance, the addition of 3.0 wt % organically modified MoS_2 (CTAB-MoS_2) enhanced the $T_{0.5}$ of PMMA by 45 °C, and reduced the PHRR value by 18.1%. 4.0 wt % graphene added into PMMA could increase the $T_{0.5}$ by 37 °C, and 1.0 wt % graphene incorporated into PMMA achieved a 32.8% increase in tensile strength and a 24.2% decrease in PHRR.[45−48]

4. CONCLUSIONS

In conclusion, a novel β-Ni(OH)$_2$ nanosheet, denoted as M-Ni(OH)$_2$, has been successfully prepared via organic-modification method. TMSAP, a new phosphorus-containing silane coupling agent, is used as the modifier. The as-fabricated M-Ni(OH)$_2$ maintains ultrathin nanosheet morphology with a small thickness of around 4.6 nm. Owning to the protection of TMSAP, thermal stability of M-Ni(OH)$_2$ is remarkably enhanced when compared to pristine β-Ni(OH)$_2$, and its interfacial property is also improved which leads to the good distribution and exfoliation morphology of M-Ni(OH)$_2$ nanosheets in the PMMA/M-Ni(OH)$_2$ nanocomposites. By adding M-Ni(OH)$_2$ ultrathin nanosheets, the mechanical performance, thermal stability, and flame retardancy of PMMA/M-Ni(OH)$_2$ nanocomposites are enhanced signifi-

DOI: 10.1021/acsami.5b04142
ACS Appl. Mater. Interfaces 2015, 7, 14603−14613

Scheme 2. Schematic Illustration for Flame-Retardant Mechanism of (a) PMMA and (b) PMMA/M-Ni(OH)$_2$ Nanocomposites

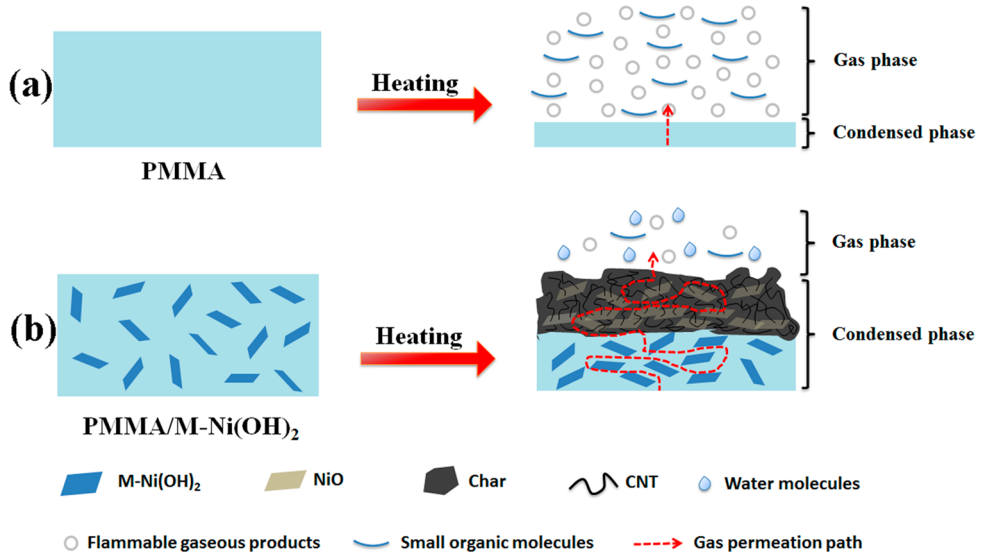

cantly, including increased storage modulus by 38.6%, $T_{0.1}$ by 42 °C and $T_{0.5}$ by 65 °C, and decreased PHRR by 25.3%. High stiffness of M-Ni(OH)$_2$ nanosheets, and the strong interfacial interaction between the nanosheets and PMMA matrix, resulted from the good distribution; exfoliation morphology and large surface areas of the nanosheets are responsible for the mechanical performance enhancement. The cooling effect and dilution effect of water molecules in the gas phase, and the physical barrier effect and catalytic charring effect of M-Ni(OH)$_2$ nanosheets in condensed phase, play key roles in the thermal stability and flame retardancy improvements. Moreover, M-Ni(OH)$_2$ nanosheets catalyze the formation of CNTs during the nanocomposite combustion, which enhance the quality of char layers; this is another positive factor for the flame retardancy enhancement. We anticipate this work not only provides a new 2D ultrathin nanomaterial with good thermal stability for polymer nanocomposites, but also will trigger more scientific interest in the development and application of new types of 2D ultrathin nanomaterials.

■ ASSOCIATED CONTENT

Supporting Information

^{1}H NMR and ^{31}P NMR spectra of TMSAP (Figure S1), and FTIR spectrum of TMSAP (Figure S2). The Supporting Information is available free of charge on the ACS Publications website at DOI: 10.1021/acsami.5b04142.

■ AUTHOR INFORMATION

Corresponding Authors

*Phone: +86-020-22236321. Fax: +86-020-22236321. E-mail: meshjiang@scut.edu.cn.

*Phone: +86-020-22236321. Fax: +86-020-22236321. E-mail: mmghchen@scut.edu.cn.

Notes

The authors declare no competing financial interest.

■ ACKNOWLEDGMENTS

This work was supported by the Natural Science Foundation of Guangdong Province (2014A030310122), the Opening Fund of Guangdong Provincial Key Laboratory of Fire Science and Technology (2013A01), and China Postdoctoral Science Foundation (2015M572309).

■ REFERENCES

(1) Choi, M.; Na, K.; Kim, J.; Sakamoto, Y.; Terasaki, O.; Ryoo, R. Stable Single-Unit-Cell Nanosheets of Zeolite MFI as Active and Long-Lived Catalysts. *Nature* **2009**, *461*, 246−249.

(2) Zhang, X.; Xie, Y. Recent Advances in Free-standing Two-Dimensional Crystals with Atomic Thickness: Design, Assembly and Transfer Strategies. *Chem. Soc. Rev.* **2013**, *42*, 8187−8199.

(3) Yu, T.; Lim, B.; Xia, Y. Aqueous-Phase Synthesis of Single-Crystal Ceria Nanosheets. *Angew. Chem., Int. Ed.* **2010**, *49*, 4484−4487.

(4) Feng, J.; Sun, X.; Wu, C.; Peng, L.; Lin, C.; Hu, S.; Yang, J.; Xie, Y. Metallic Few-Layered VS_2 Ultrathin Nanosheets: High Two-Dimensional Conductivity for In-Plane Supercapacitors. *J. Am. Chem. Soc.* **2011**, *133*, 17832−17838.

(5) Huang, X.; Zeng, Z.; Zhang, H. Metal Dichalcogenide Nanosheets: Preparation, Properties and Applications. *Chem. Soc. Rev.* **2013**, *42*, 1934−1946.

(6) Lin, C.; Zhu, X.; Feng, J.; Wu, C.; Hu, S.; Peng, J.; Guo, Y.; Peng, L.; Zhao, J.; Huang, J.; Yang, J.; Xie, Y. Hydrogen-Incorporated TiS_2 Ultrathin Nanosheets with Ultrahigh Conductivity for Stamp-Transferrable Electrodes. *J. Am. Chem. Soc.* **2013**, *135*, 5144−5151.

(7) Yin, Z.; Li, H.; Li, H.; Jiang, L.; Shi, Y.; Sun, Y.; Lu, G.; Zhang, Q.; Chen, X.; Zhang, H. Single-Layer MoS_2 Phototransistors. *ACS Nano* **2012**, *6*, 74−80.

(8) Xu, K.; Chen, P.; Li, X.; Wu, C.; Guo, Y.; Zhao, J.; Wu, X.; Xie, Y. Ultrathin Nanosheets of Vanadium Diselenide: a Metallic Two-Dimensional Material with Ferromagnetic Charge-Density-Wave Behavior. *Angew. Chem., Int. Ed.* **2013**, *52*, 10477−10481.

(9) Shi, Y.; Jiang, S.; Zhou, K.; Bao, C.; Yu, B.; Qian, X.; Wang, B.; Hong, N.; Wen, P.; Gui, Z.; Hu, Y.; Yuen, R. K. K. Influence of g-C_3N_4 Nanosheets on Thermal Stability and Mechanical Properties of Biopolymer Electrolyte Nanocomposite Films: a Novel Investigation. *ACS Appl. Mater. Interfaces* **2014**, *6*, 429−437.

(10) Matusinovic, Z.; Shukla, R.; Manias, E.; Hogshead, C. G.; Wilkie, C. A. Polystyrene/Molybdenum Disulfide and Poly(methyl methacrylate)/Molybdenum Disulfide Nanocomposites with Enhanced Thermal Stability. *Polym. Degrad. Stab.* **2012**, *97*, 2481−2486.

(11) Ramanathan, T.; Abdala, A. A.; Stankovich, S.; Dikin, D. A.; Herrera-Alonso, M.; Piner, R. D.; Adamson, D. H.; Schniepp, H. C.; Chen, X.; Ruoff, R. S.; Nguyen, S. T.; Aksay, I. A.; Prud'homme, R. K.; Brinson, L. C. Functionalized Graphene Sheets for Polymer Nanocomposites. *Nat. Nanotechnol.* **2008**, *3*, 327−331.

DOI: 10.1021/acsami.5b04142
ACS Appl. Mater. Interfaces 2015, 7, 14603−14613

(12) Xing, S.; Wang, Q.; Ma, Z.; Wu, Y.; Gao, Y. Controlled Synthesis of Mesoporous Beta-Ni(OH)(2) and NiO Nanospheres with Enhanced Electrochemical Performance. *Mater. Res. Bull.* **2012**, *47*, 2120−2125.
(13) Minmin, W.; Wanzhong, R.; Yunan, Z.; Yan, L.; Hongtao, C. One-Pot Synthesis of Powder-Form Beta-Ni$(OH)_2$ Monolayer Nanosheets with High Electrochemical Performance. *J. Nanopart. Res.* **2013**, *15*, 1849−1849.
(14) Wang, H.; Casalongue, H. S.; Liang, Y.; Dai, H. Ni(OH)(2) Nanoplates Grown on Graphene as Advanced Electrochemical Pseudocapacitor Materials. *J. Am. Chem. Soc.* **2010**, *132*, 7472−7477.
(15) Li, G.; Wang, X.; Ding, H.; Zhang, T. A Facile Synthesis Method for Ni$(OH)_2$ Ultrathin Nanosheets and their Conversion to Porous NiO Nanosheets Used for Formaldehyde Sensing. *RSC Adv.* **2012**, *2*, 13018−13023.
(16) Ida, S.; Shiga, D.; Koinuma, M.; Matsumoto, Y. Synthesis of Hexagonal Nickel Hydroxide Nanosheets by Exfoliation of Layered Nickel Hydroxide Intercalated with Dodecyl Sulfate Ions. *J. Am. Chem. Soc.* **2008**, *130*, 14038−14039.
(17) Hong, D. C.; Yamada, Y.; Nagatomi, T.; Takai, Y.; Fukuzumi, S. Catalysis of Nickel Ferrite for Photocatalytic Water Oxidation Using [Ru(bpy)3]2+ and S2O82-. *J. Am. Chem. Soc.* **2012**, *134*, 19572−19575.
(18) Liang, X.; Xiao, J. J.; Gou, Y.; Chen, B. H. Synthesis and Catalysis Properties of NiO Flower-like Spheres and Nanosheets: Water-Induced Phase Transformation of Nickel Hydroxides. *J. Mater. Res.* **2011**, *26*, 3091−3097.
(19) Tasker, S. Z.; Standley, E. A.; Jamison, T. F. Recent Advances in Homogeneous Nickel Catalysis. *Nature* **2014**, *509*, 299−309.
(20) Wu, J. L.; Xia, Q. B.; Wang, H. H.; Li, Z. Catalytic Performance of Plasma Catalysis System with Nickel Oxide Catalysts on Different Supports for Toluene Removal: Effect of Water Vapor. *Appl. Catal., B* **2014**, *156*, 265−272.
(21) Hong, N.; Tang, G.; Wang, X.; Hu, W.; Song, L.; Hu, Y. Selective Preparation of Carbon Nanoflakes, Carbon Nanospheres, and Carbon Nanotubes through Carbonization of Polymethacrylate by Using Different Catalyst Precursors. *J. Appl. Polym. Sci.* **2013**, *130*, 1029−1037.
(22) Jiang, Z.; Song, R.; Bi, W.; Lu, J.; Tang, T. Polypropylene as a Carbon Source for the Synthesis of Multi-Walled Carbon Nanotubes via Catalytic Combustion. *Carbon* **2007**, *45*, 449−458.
(23) Hong, N.; Wang, B.; Song, L.; Hu, S.; Tang, G.; Wu, Y.; Hu, Y. Low-cost, Facile Synthesis of Carbon Nanosheets by Thermal Pyrolysis of Polystyrene Composite. *Mater. Lett.* **2012**, *66*, 60−63.
(24) Hong, N.; Nie, S.; Song, L.; Tai, Q.; Zhang, P.; Wang, B.; Qian, X.; Hu, Y. Controllable Synthesis of Multi-layer Graphene Flakes and Multi-wall Carbon Nanotubes from Pyrolyzing Biodegradable Poly-(butylene succinate) Composites. *Mater. Lett.* **2011**, *65*, 2707−2710.
(25) Meng, X.; Jiang, Z.; Bi, W.; Academy, C. Catalyzing Carbonization of Polypropylene itself by Supported Nickel Catalyst during Combustion of Polypropylene/Clay Nanocomposite for Improving Fire Retardancy. *Chem. Mater.* **2005**, *17*, 2799−2802.
(26) Chung, Y. H.; Jou, S. Carbon Nanotubes from Catalytic Pyrolysis of Polypropylene. *Mater. Chem. Phys.* **2005**, *92*, 256−259.
(27) Kashiwagi, T.; Du, F. M.; Douglas, J. F.; Winey, K. I.; Harris, R. H.; Shields, J. R. Nanoparticle Networks Reduce the Flammability of Polymer Nanocomposites. *Nat. Mater.* **2005**, *4*, 928−933.
(28) Liang, Z. H.; Zhu, Y. J.; Hu, X. L. Beta-Nickel Hydroxide Nanosheets and their Thermal Decomposition to Nickel Oxide Nanosheets. *J. Phys. Chem. B* **2004**, *108*, 3488−3491.
(29) Zhu, J. X.; Gui, Z.; Ding, Y. Y.; Wang, Z. Z.; Hu, Y.; Zou, M. Q. A Facile Route to Oriented Nickel Hydroxide Nanocolumns and Porous Nickel Oxide. *J. Phys. Chem. C* **2007**, *111*, 5622−5667.
(30) Jiang, S.; Yu, B.; Zhou, K.; Yang, H.; Shi, Y.; Lo, S.; Hu, Y.; Gui, Z. Sol-gel Synthesis and Enhanced Properties of a Novel Transparent PMMA Based Organic-Inorganic Hybrid Containing Phosphorus, Nitrogen and Silicon. *J. Sol-Gel Sci. Technol.* **2014**, *69*, 418−428.
(31) Zha, C.; Wang, W.; Lu, Y.; Zhang, L. Constructing Covalent Interface in Rubber/Clay Nanocomposite by Combining Structural Modification and Inter Lamellar Silylation of Montmorillonite. *ACS Appl. Mater. Interfaces* **2014**, *6*, 18769−18779.
(32) Qian, X. D.; Yu, B.; Bao, C. L.; Song, L.; Wang, B. B.; Xing, W. Y.; Hu, Y.; Yuen, R. K. K. Silicon Nanoparticle Decorated Graphene Composites: Preparation and Their Reinforcement on the Fire Safety and Mechanical Properties of Polyurea. *J. Mater. Chem. A* **2013**, *1*, 9827−9836.
(33) Sarkar, S.; Pradhan, M.; Sinha, A. K.; Basu, M.; Negishi, Y.; Pal, T. An Aminolytic Approach toward Hierarchical Beta-Ni$(OH)_2$ Nanoporous Architectures: a Bimodal Forum for Photocatalytic and Surface-Enhanced Raman Scattering Activity. *Inorg. Chem.* **2010**, *49*, 8813−8827.
(34) Kotal, M.; Srivastava, S. K. Synergistic Effect of Organo-modification and Isocyanate Grafting of Layered Double Hydroxide in Reinforcing Properties of Polyurethane Nanocomposites. *J. Mater. Chem.* **2011**, *21*, 18540−18551.
(35) Tai, Q.; Song, L.; Hu, Y.; Yuen, R. K. K.; Feng, H.; Tao, Y. Novel Styrene Polymers Functionalized with Phosphorus-Nitrogen Containing Molecules: Synthesis and Properties. *Mater. Chem. Phys.* **2012**, *134*, 163−169.
(36) Zhao, J.; Yang, M.; Hua, Z. Synthesis and Magnetic Properties of Beta-Ni$(OH)_2$ and NiO Nanosheets. *J. Magn. Magn. Mater.* **2014**, *371*, 10−13.
(37) Yeh, J. M.; Chang, K. C.; Peng, C. W.; Lai, M. C.; Hung, C. B.; Hsu, S. C.; Hwang, S. S.; Lin, H. R. Effect of Dispersion Capability of Organoclay on Cellular Structure and Physical Properties of PMMA/Clay Nanocomposite Foams. *Mater. Chem. Phys.* **2009**, *115*, 744−750.
(38) Wang, G. A.; Wang, C. C.; Chen, C. Y. The Disorderly Exfoliated LDHs/PMMA Nanocomposites Synthesized by In Situ Bulk Polymerization: The Effects of LDH-U on Thermal and Mechanical Properties. *Polym. Degrad. Stab.* **2006**, *91*, 2443−2450.
(39) Park, H. M.; Lee, W. K.; Park, C. Y.; Cho, W. J.; Ha, C. S. Environmentally Friendly Polymer Hybrids - Part I - Mechanical, Thermal, and Barrier Properties of Thermoplastic Starch/Clay Nanocomposites. *J. Mater. Sci.* **2003**, *38*, 909−915.
(40) Qin, H. L.; Su, Q. S.; Zhang, S. M.; Zhao, B.; Yang, M. S. Thermal Stability and Flammability of Polyamide 66/Montmorillonite Nanocomposites. *Polymer* **2003**, *44*, 7533−7538.
(41) Shi, Y.; Kashiwagi, T.; Walters, R. N.; Gilman, J. W.; Lyon, R. E.; Sogah, D. Y. Ethylene Vinyl Acetate/Layered Silicate Nanocomposites Prepared by a Surfactant-free Method: Enhanced Flame Retardant and Mechanical Properties. *Polymer* **2009**, *50*, 3478−3487.
(42) Chen, X. L.; Jiao, C. M. Flammability and Thermal Degradation of Epoxy Acrylate Modified with Phosphorus-containing Compounds. *Polym. Adv. Technol.* **2010**, *21*, 490−495.
(43) Lu, H.; Song, L.; Hu, Y. A Review on Flame Retardant Technology in China. Part II: Flame Retardant Polymeric Nanocomposites and Coatings. *Polym. Adv. Technol.* **2011**, *22*, 379−394.
(44) Dervishi, E.; Li, Z.; Watanabe, F.; Courte, A.; Biswas, A.; Biris, A. R.; Saini, V.; Xu, Y.; Biris, A. S. Versatile Catalytic System for the Large-Scale and Controlled Synthesis of Single-Wall, Double-Wall, Multi-Wall, and Graphene Carbon Nanostructures. *Chem. Mater.* **2009**, *21*, 5491−5498.
(45) Huang, G. B.; Chen, S. Q.; Song, P. G.; Lu, P. P.; Wu, C. L.; Liang, H. D. Combination Effects of Graphene and Layered Double Hydroxides on Intumescent Flame-retardant Poly(methyl methacrylate) Nanocomposites. *Appl. Clay Sci.* **2014**, *88*−*89*, 78−85.
(46) Zhou, K. Q.; Liu, J. J.; Zeng, W. R.; Hu, Y.; Gui, Z. In Situ Synthesis, Morphology, and Fundamental Properties of Polymer/MoS_2 Nanocomposites. *Compos. Sci. Technol.* **2015**, *107*, 120−128.
(47) Fan, Z.; Gong, F.; Nguyen, S. T.; Duong, H. M. Advanced Multifunctional Graphene Aerogel - Poly(methyl methacrylate) Composites: Experiments and Modeling. *Carbon* **2015**, *81*, 396−404.
(48) Sheng, X.; Xie, D.; Cai, W.; Zhang, X.; Zhong, L.; Zhang, H. In Situ Thermal Reduction of Graphene Nanosheets Based Poly(methyl methacrylate) Nanocomposites with Effective Reinforcements. *Ind. Eng. Chem. Res.* **2015**, *54*, 649−658.

DOI: 10.1021/acsami.5b04142
ACS Appl. Mater. Interfaces 2015, 7, 14603−14613